Thermoelectric phonon-glass electron-crystal via ion beam patterning of silicon

Taishan Zhu, Krishnan Swaminathan-Gopalan, Kelly Stephani, and Elif Ertekin*
Department of Mechanical Science and Engineering, University of Illinois at Urbana-Champaign, Urbana, Illinois 61820, USA

(Received 8 October 2017; revised manuscript received 27 February 2018; published 1 May 2018)

Ion beam irradiation has recently emerged as a versatile approach to functional materials design. We show in this work that patterned defective regions generated by ion beam irradiation of silicon can create a phonon-glass electron-crystal (PGEC), a long-standing goal of thermoelectrics. By controlling the effective diameter of and spacing between the defective regions, molecular dynamics simulations suggest a reduction of the thermal conductivity by a factor of ∼20 is achievable. Boltzmann theory shows that the thermoelectric power factor remains largely intact in the damaged material. To facilitate the Boltzmann theory, we derive an analytical model for electron scattering with cylindrical defective regions based on partial-wave analysis. Together we predict a figure of merit of $ZT \approx 0.5$ or more at room temperature for optimally patterned geometries of these silicon metamaterials. These findings indicate that nanostructuring of patterned defective regions in crystalline materials is a viable approach to realize a PGEC, and ion beam irradiation could be a promising fabrication strategy.

DOI: 10.1103/PhysRevB.97.174201

I. INTRODUCTION

Since their discovery, thermoelectric materials have attracted extensive interest for direct conversion between heat and electrical energy via Seebeck/Peltier effects [1–5]. As opposed to fossil fuels, thermoelectrics are pollution free during operation, are stable, and have decent manufacturing scalability [2,5]. Nevertheless, the thermoelectric conversion efficiency must be enhanced for large-scale future adoption [1–5]. The conversion efficiency is given by [6]

$$\eta = \eta_C \frac{\sqrt{ZT+1}-1}{\sqrt{ZT+1}+T_H/T_C}, \qquad (1)$$

which, as the figure of merit $ZT = \sigma S^2 T/\kappa$ increases, approaches the Carnot efficiency η_C of an engine operating between heat baths with temperatures T_H and T_C. Here σ is the electrical conductivity, S is the Seebeck coefficient, and κ is the total thermal conductivity, which aggregates contributions from electrons and phonons. Since σ, S, and κ are intrinsically related material parameters, they must be carefully coordinated in order to achieve a high ZT.

To this end, early efforts focused separately on either *thermal* or *electrical* properties [6]. While κ can be reduced by phonon engineering [7], the power factor $S^2\sigma$ can be enhanced by doping and electron band structure engineering such as in low-dimensional materials and nanostructures [8,9]. In the 1990s, the separate approaches were merged, culminating in the notion of the phonon-glass electron-crystal (PGEC) [10], in which a material is perceived as glassy by phonons but remains crystalline for electrons. To realize a phonon-glass electron-crystal, several approaches have proven promising. First, scattering of phonons via disorder, such as by alloying, rattler structures, and point defects, has been demonstrated. The alloying approach has recently achieved a high $ZT \approx 2.3$ for iodine-doped Cu_2Se [11]. Second, scattering of phonons through nanostructuring such as superlattices and nanowires can also be effective. A $ZT \approx 2.4$ was reported in p-type Bi_2Te_3/Sb_2Te_3 superlattices at room temperature [12,13]. Third, complex crystals are now emerging [14], including skutterudites [15] and half-Heusler alloys [16]. The κ of these compounds is often below 5 W/mK, comparable to glasses, contributing to a ZT around unity [14]. If only material performance were relevant, these recently reported examples would already be quite competitive.

However, for thermoelectric deployment at global scales, it is imperative to account for material cost and scalability of manufacturing [2,17]. Most notable thermoelectric materials contain elements such as Bi, Te, Sb, Pb, and Ag, which are either expensive, toxic, or challenging for processing. By contrast, silicon, the most widely used material, is nowadays being reconsidered as a promising candidate [17–20]. Due to its low cost and viable manufacturability, investigations into thermoelectric applications [21] in both bulk alloy and nanostructured form [17,19] have regained interest. For instance, bulk $Si_{0.98}Ge_{0.02}$ has an appealing $ZT \sim 0.32$ at the competitive price of US$1.7/W [19].

In this work, we propose a silicon nanocomposite composed of regularly patterned defective regions embedded in a crystalline host, as shown in Fig. 1(a), for thermoelectric applications. In our recent work [22], we directly simulated the ion beam irradiation process using molecular dynamics and showed that the effective diameter of defective regions D and the spacing between them L can be controlled by varying the parameters of the ion beam irradiation process, such as ion type, irradiation energy, fluence, beam diameter, and beam incidence angle. The system considered here shares some features with other recently proposed concepts for patterned silicon, such as nanoporous silicon [20], holey silicon [23], and silicon nanomeshes [24]. Whereas most of these have concentrated on structuring at the scale of several atomic spacings, the systems considered here extend to larger length

*Corresponding author: ertekin@illinois.edu

 ©2018 American Physical Society

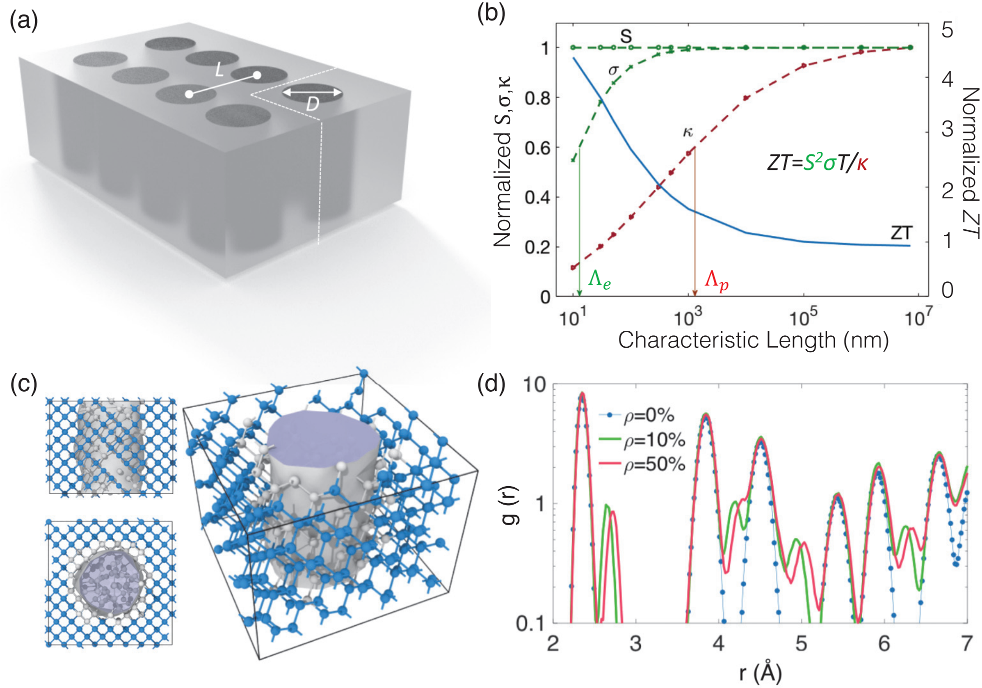

FIG. 1. (a) Schematic of silicon metamaterial for thermoelectric applications, where the dark areas denote damaged domains patterned by ion beam irradiation. (b) The rationale for the patterned system, in which electrical properties are expected to increase towards the bulk values faster than thermal properties with increasing feature size as a result of the different phonon and electron mean free paths. If the feature size is larger than the electron mean free path Λ_e and smaller than the phonon mean free path Λ_p, ZT can be enhanced. (c) A representative supercell for (a) in atomic view, with disordered regions generated by ion beam irradiation, obtained with molecular dynamics simulations. (d) The radial distribution function for the specimens shown in (a) and (c). New peaks and fine shifts can be observed as the degree of disorder ρ increases.

scales that lie between the mean free path of electrons and that of phonons. The physical justification for the proposed metamaterial is illustrated conceptually in Fig. 1(b). Due to the long phonon mean free paths Λ_p in silicon relative to the corresponding electron mean free paths Λ_e, we expect that as the nanostructure feature size grows, the electronic conductivity will increase and saturate more quickly than the thermal conductivity. If the interdefective region distance L falls within the length window spanned by the mean free path of electrons Λ_e and that of phonons Λ_p, then κ can be reduced due to phonon scattering while σ is largely retained, and thereby ZT can be enhanced.

The purpose of the present work is to verify that the proposed metamaterial formed by ion beam patterning of silicon can lead to a PGEC. Atomic simulations are performed to determine the phonon transport and thermal conductivity, while the Boltzmann transport theory is employed to estimate the electrical properties. Whereas Green-Kubo calculations have been well established for obtaining thermal conductivity, the scattering model for electrons with the cylindrical defective regions is currently not available in the literature. To bridge this gap, we derive an analytical scattering model based on the partial-wave approach and gas-kinetic theory, which combines quantum and classical transport theories (a similar model for scattering with quantum dots was proposed recently in Ref. [25]). The scattering model is based on perturbation theory and expected to be valid for low-energy, independent carrier scattering events. Using this scattering model, we demonstrate that it is possible to achieve a substantial reduction in κ without sacrificing electrical properties and predict that $ZT \approx 0.5$ or greater is achievable. This compares well with other nanostructured silicon systems reported in the literature such as silicon nanowires ($ZT \approx 1$) [18,26] and nanoporous silicon ($ZT \approx 0.4$) [20,23] but, practically, has the advantage of ease of manufacturability via ion beam irradiation.

II. COMPUTATIONAL METHODS AND THEORETICAL MODELS

To study the thermoelectric transport properties, we used different techniques for phonons and electrons. For the prediction of thermal conductivity, we applied Green-Kubo formalism implemented in equilibrium molecular dynamics simulations. Meanwhile, for electrical properties, we resorted to Boltzmann theory and the relaxation-time approximation.

A. Equilibrium molecular dynamics for κ

The ion-beam-irradiated materials are created by direct simulation of ion bombardments using molecular dynamics simulations, as described in detail in our previous work [22]. The impact location is randomly chosen from a two-dimensional normal distribution parameterized by beam diameter, which mimics a focused ion beam apparatus. As annealing is expected to be most prominent in the first few picoseconds after ion impact, we allow the system to anneal for 70 ps at $T = 300$ K between two consecutive ion impacts. An ensemble of 50 independent irradiation processes is simulated to obtain satisfactory

statistics. All molecular dynamics calculations were performed using HOOMD-blue [27]. The interactions between silicon atoms are described by the Tersoff potential [28], and ion-Si interactions are described by the Ziegler-Biersack-Littmark universal repulsive potential [29]. Figure 1(c) illustrates an example of a sample irradiated by a 5 keV Xe ion beam oriented normal to the surface. The damaged region is characterized as a cylindrical region with the diameter describing the radial extent and height describing the range of damage [see Fig. 1(c)]. The corresponding radial distribution function for varying degrees of disorder is shown in Fig. 1(d), where new peaks are generated due to the presence of disorder, which drift as the degree of disorder increases.

The thermal conductivity κ of the irradiated samples is calculated using the Green-Kubo formulism [30], which relates κ to the fluctuation of heat flux,

$$\kappa = \frac{1}{k_B V T^2} \int_0^\infty \langle \boldsymbol{J}(t) \cdot \boldsymbol{J}(0) \rangle dt, \tag{2}$$

based on the fluctuation-dissipation theorem. Here k_B is the Boltzmann constant, V is volume, t is time, and $\langle \boldsymbol{J}(t) \cdot \boldsymbol{J}(0) \rangle$ is the autocorrelation function of heat current $\boldsymbol{J}$ calculated from molecular dynamics simulations. The integral is considered converged once the statistical errors fall within 5%. All simulations were performed at $T = 300$ K with a time step of 0.5 fs. The system was equilibrated to the desired temperature for 20 ps with a Berendsen thermostat and then sampled in the microcanonical ensemble for an additional 20 ps. The heat current was then recorded for a simulation time of 6 ns. For each value of κ reported below, ten independent microstates are simulated, and κ is averaged over in-plane directions $\kappa = (\kappa_x + \kappa_y)/2$. The calculated κ of pristine silicon at room temperature is approximately 270 W/mK from this method, almost twice that of the experimentally observed value of 150 W/mK [31]. However, this numerical value is consistent with other molecular simulations using the same potential [32].

B. Boltzmann theory for σ, S

For the electronic properties σ and S we have applied Boltzmann theory. We use the relaxation-time approximation and the parabolic-band approximation for the electronic dispersion. These approximations are sufficiently accurate for nondegenerately doped silicon since at typical thermoelectric operating temperatures ($T = 300$ K to $T = 700$ K) the filling of the conduction bands is relatively small [33,34]. Within this framework the kinetic definitions of σ and S are given by [6]

$$\sigma = -q^2 \int v(\epsilon)^2 \tau(\epsilon) \frac{\partial f}{\partial \epsilon} g(\epsilon)\, d\epsilon, \tag{3}$$

$$S = \frac{1}{qT} \frac{\int v(\epsilon)^2 \tau(\epsilon) \frac{\partial f}{\partial \epsilon} [\epsilon - \mu] g(\epsilon)\, d\epsilon}{\int v(\epsilon)^2 \tau(\epsilon) \frac{\partial f}{\partial \epsilon} g(\epsilon)\, d\epsilon}, \tag{4}$$

where q is the elementary charge, ϵ is the charge carrier energy, $v(\epsilon)^2 = 2\epsilon/m^*$ is the group velocity squared, m^* is the carrier effective mass, $\tau(\epsilon)$ is the relaxation time, $f(\epsilon) = [e^{(\epsilon-\mu)/k_B T} + 1]^{-1}$ is the Fermi-Dirac distribution, μ is the chemical potential, and $g(\epsilon) = \sqrt{2}\pi^{-2}\hbar^{-3}(m^*)^{3/2}\epsilon^{1/2}$ is the electronic density of states. A factor of 2 accounting for spins has been absorbed into the density of states. We consider donor doping by phosphorous (activation energy of 45 meV) at a concentration of 3×10^{19} cm^{-3}. The resulting carrier density and Fermi level are determined self-consistently via a graphical iteration method (see Ref. [35] and Appendix A). The relaxation time $\tau(\epsilon)$ remains the only unknown to be determined.

To determine $\tau(\epsilon)$, we consider intrinsic and extrinsic scattering processes, with the latter arising here directly from the damaged regions created by ion beam irradiation. Matthiessen's law gives the overall scattering rate as

$$\tau_0^{-1}(\epsilon) = \tau_i^{-1}(\epsilon) + \tau_D^{-1}(\epsilon), \tag{5}$$

where $\tau_i(\epsilon)$ denotes intrinsic and $\tau_D(\epsilon)$ denotes extrinsic scattering times. This amounts to assuming that the defective regions act as isolated scattering centers. For $\tau_i(\epsilon)$, we assume that in the irradiated samples the intrinsic scattering mechanisms remain unchanged from pristine silicon [33], a commonly used assumption when studying nanostructured thermoelectric metamaterials [20]. We incorporate descriptions of intrinsic electron scattering according to the deformation potential of acoustic phonons and optical phonons; all the material parameters and models are summarized in Table I. Scattering rates for both acoustic and optical phonons share the power-law form $\tau_i(\epsilon) = \tau_{i0}(\epsilon/k_B T)^r$, where the parameters τ_{i0} and r can be fitted to experimental measurements and have previously been well characterized for silicon [36].

On the other hand, in order to determine $\tau_D(\epsilon)$, we invoked the partial-wave approach. Partial-wave analysis is a general method to calculate scattering cross sections applicable when the scattering potential is azimuthally symmetric [38], which is an approximate but reasonable description of the

TABLE I. The scattering mechanisms and corresponding power-law models, $\tau_i(\epsilon) = \tau_{i0} x^{r_i}, x = \epsilon/k_B T$, considered in this work. The dominant scattering mechanisms around and above room temperature are deformation-potential scattering with acoustic and optical phonons. The parameters are obtained by fitting experimental measurements [36,37]: $D_A = 9.0$ eV, $C_l = (3C_{11} + 2C_{12} + 4C_{44})/5 = 1.895 \times 10^7$ Pa, $\theta = \hbar\omega_{LO}/k_B = 731.1$ K, $m = 9.11 \times 10^{-31}$ kg denotes the electron mass, and $m^* = 0.26m$ is the conductivity effective mass. Note that the unified power law with identical exponents r_i largely simplifies the analysis in this work.

Scattering mechanism i	τ_{i0}	r_i	Refs.
Acoustic phonon deformation potential	$\frac{2.40\times10^{-19} C_l}{D_A^2 T^{3/2}} \left(\frac{m}{m^*}\right)^{3/2}$	$-1/2$	[36,37]
Optical phonon deformation potential	$\frac{4.83\times10^{-19} C_l [\exp(\theta/T)-1]}{D_A^2 T^{1/2}\theta} \left(\frac{m}{m^*}\right)^{3/2}$	$-1/2$	[36,37]
Cylindrical defective area	$\frac{\pi}{4\sqrt{2}} \frac{L^2}{D} \sqrt{\frac{m^*}{k_B T}}$	$-1/2$	Eq. (12) in this work

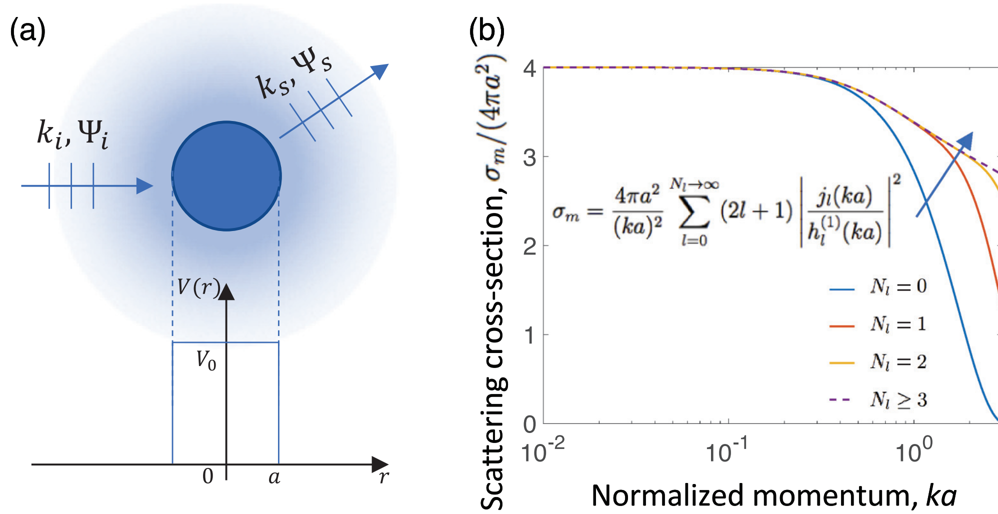

FIG. 2. (a) Schematic of the scattering model for calculating the scattering cross section and scattering time with cylindrical defective area. (b) The convergence of the exact solution to the infinite scattering barrier with the number of partial waves N_l considered. For $ka < 0.5$ the S wave ($N_l = 0, l = 0$) is sufficient for accurate descriptions of the scattering cross section.

ion-beam-damaged regions. This approach has been applied recently to estimate the scattering time for electrons interacting with spherical quantum dots embedded in a host matrix [25]. In the following section, we adapt the method to cylindrical, rather than spherical, defective regions of interest here. This theoretical scattering model will also be applicable to other recently proposed planar-patterned nanomaterials [39] and two-dimensional nanoporous/holey metamaterials [40,41].

C. Relaxation time $\tau_D(\epsilon)$ due to cylindrical defects

In the following we derive the scattering rate for electrons $\tau_D(\epsilon)$ due to the presence of a cylindrical barrier potential, as shown in Fig. 2(a),

$$V(r) = \begin{cases} V_0, & r \leqslant a, \\ 0, & r > a, \end{cases} \tag{6}$$

where $V_0 > 0$ is the barrier height. Assuming the scattering is elastic, kinetic theory [42] gives

$$\tau_D(\epsilon)^{-1} = N_D \langle v \rangle D_m, \tag{7}$$

where N_D is the density of defected regions, $\langle v \rangle$ is the average carrier velocity, $D_m = \sqrt{4\sigma_m/\pi}$ is the scattering diameter, and σ_m denotes the momentum scattering cross section defined by

$$\sigma_m = \int \sigma(\theta)(1 - \cos\theta) d\Omega$$
$$= 2\pi \int_0^{\pi} \sigma(\theta)(1 - \cos\theta) \sin\theta d\theta, \tag{8}$$

where $\sigma(\theta) = \frac{d\sigma}{d\Omega}$ is the differential scattering cross section that measures the probability of incident particles passing through an infinitesimal area $d\sigma$ and then being scattered into solid angle $d\Omega$. Here the differential cross section is independent of azimuthal angle due to the potential symmetry. The description based on kinetic theory here relies on the assumptions that scattering events are independent and that carriers can be described as particles in the classical limit.

A detailed derivation of the scattering cross section using partial-wave analysis is provided in Appendix B. In the limit of the low-energy elastic scattering process, the cross section is

$$\sigma_m \approx 4\pi a^2 \left(1 - \frac{\tanh(k_0 a)}{k_0 a}\right)^2 \approx 4\pi a^2, \tag{9}$$

which is an approximate solution obtained by retaining only the S-wave ($l = 0$) component of the complete solution

$$\sigma_m = \frac{4\pi a^2}{(ka)^2} \sum_{l=0}^{N_l \to \infty} (2l+1) \left| \frac{j_l(ka)}{h_l^{(1)}(ka)} \right|^2, \tag{10}$$

where j_l and $h_l^{(1)}$ are the spherical Bessel and first-kind Hankel functions, $k^2 = 2m\epsilon/\hbar^2$, and $k_0^2 = 2mV_0/\hbar^2$. An *a posteriori* justification of the assumed S-wave scattering, with higher-order terms neglected, is presented in Fig. 2(b). In the limit of an insulating, impermeable defective region ($V_0 \to \infty$), the boundary condition becomes $\psi(a,\theta) = 0$. As seen from Fig. 2(b), the calculated cross section converges quickly with the number of angular terms N_l included. For instance, when $ka = 0.5$ with only $l = 0$, an error of 1.91% is introduced. Therefore, retaining the $l = 0$ term alone well represents low-energy scattering ($ka \ll 1$).

Before substituting Eq. (9) into Eq. (7) to obtain the scattering rate, the average velocity of incident carriers must be found. Within the parabolic band description adopted here, the carrier speed is related to the energy as $v = \sqrt{2\epsilon/m^*}$. Due to the uniform distribution of angles $\vartheta \in [-\pi/2, \pi/2]$ between the velocity vector and the longitudinal cylinder axis, the average incident speed is

$$\langle v \rangle = \int_{-\pi/2}^{\pi/2} v \cos\vartheta \, \Theta(\vartheta) d\vartheta = \frac{2v}{\pi}, \tag{11}$$

with the distribution density $\Theta(\vartheta) = 1/\pi$.

Combining Eqs. (7), (9), and (11) and letting $N_D = 1/L^2$ be the number density of the defective areas, the momentum

relaxation time can be written as

$$\tau_D(\epsilon)^{-1} = N_D \langle v \rangle D_m = \frac{4\sqrt{2}}{\pi}\frac{D}{L^2}\sqrt{\frac{k_B T}{m^*}}x^{1/2}, \qquad (12)$$

where $x = \epsilon/k_B T$. Ultimately, the external scattering rate due to the cylindrical defective areas exhibits the power-law form $\tau_D(\epsilon) = \tau_{D0}(\epsilon/k_B T)^r$ with the exponent $r = 1/2$, which turns out to be the same scaling as in all intrinsic models (see Table I). The unified power-law scattering conveniently simplifies our analysis, allowing a unified calculation of electrical properties. Substituting $\tau(\epsilon) = (\tau_{i0} + \tau_{D0})(\epsilon/k_B T)^r$, $r = 1/2$, into Eqs. (3) and (4),

$$\sigma = \frac{2q^2\tau_0(3/2 + r)(k_B T)^{3/2+r}\Gamma(3/2 + r)}{3\sqrt{2}\pi^{3/2}\Gamma(3/2)}(m^*)^{1/2}e^{\eta}, \qquad (13)$$

$$S = -\frac{k_B}{q}\left(\eta - r - \frac{5}{2}\right), \qquad (14)$$

where Γ denotes the gamma function and $\eta = \mu/(k_B T)$ is the reduced chemical potential.

Although this model assumes that scattering events occur independently, we expect it to capture the transport physics sufficiently. On the one hand, the near-field detailed interactions could be resolved by adding more components in the partial-wave expansion. In principle, the expansion could achieve arbitrary accuracy by introducing more terms. However, we take only the s-wave component in our model, which simplifies our analysis and provides satisfactory accuracy (see Fig. 2). The assumption of independent scattering events would break down if resonance effects, which would affect the carriers within a narrow modal window, were to become dominant. It would also break down if higher-order inelastic scattering effects are significant, such as when electron energy and/or temperature are high. The analysis here is therefore limited to low-energy scattering.

It is also important to note that our model for electron scattering does not consider the atomic details of the defective region, which may include dangling bonds and reconstructions. However, the approach is expected to be a reasonable approximation since, first, the geometric parameters D and L are directly controllable through the ion beam irradiation process. These two parameters are statistically obtained mean values from our atomistic simulations. Fine structural features, such as reconstruction and dangling bonds, are higher-order perturbations to the defective region. Second, we model the limiting case where the defective area is considered to be completely electrically insulating. Therefore, it is likely that the electronic conductivity reported here underestimates actual values. Although reconstruction and dangling bonds may affect the electrical conductivity in practice, the effect would be small near the insulating limit considered here.

III. RESULTS AND DISCUSSION

A. Thermoelectric properties of defective silicon metamaterials

Using the equilibrium molecular dynamics simulations, we predict κ as a function of the geometric parameters D and L, as summarized in Fig. 3(a). The thermal conductivity of the irradiated metamaterials is suppressed appreciably compared to pristine silicon. For instance, with $L = 11$ nm and $D = 5$ nm, κ is reduced by a factor of 19 from 270 W/mK for crystalline silicon. In our recent work combining lattice dynamics and molecular dynamics, this reduction in κ is found to arise largely from hybridization, interactions, and avoided crossings between bulklike vibrational modes and modes confined to the defective regions [43]. As L increases, κ is expected to approach the numerical value of 270 W/mK for bulk silicon. The lattice conductivity in Fig. 3(a) shows high sensitivity to the interdefect distance L and is less sensitive to the defect diameter D (discussed further below).

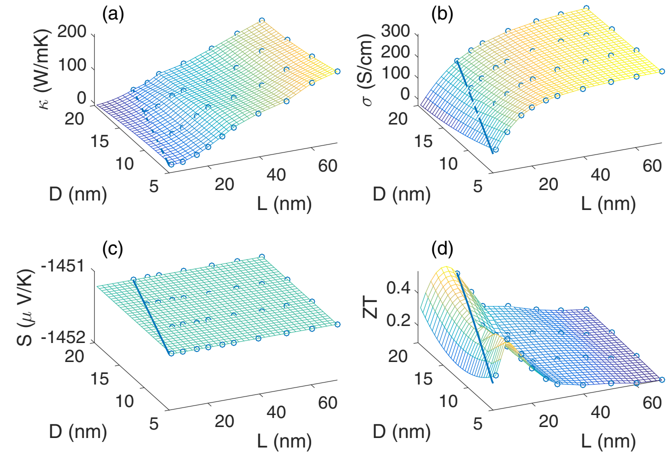

FIG. 3. (a) Thermal conductivity κ, (b) electrical conductivity σ, (c) Seebeck coefficient S, and (d) figure of merit ZT as a function of D and L for n-type silicon doped at a concentration of 3×10^{19} cm^{-3} at room temperature. Both σ and κ are more sensitive to L than D. Electron conductivity σ grows quickly and saturates sooner than thermal conductivity κ with L, which allows the patterned metamaterial to be more crystalline for electrons than for phonons. For $T = 300$ K at the given dopant concentration, ZT can be enhanced to around $ZT \approx 0.5$ for optimal $L \approx 11$ nm, $D \approx 5$ nm. The thick blue lines correspond to $L = D$; the regions to the left of the lines are geometrically unphysical.

The electrical properties σ and S are plotted similarly as functions of L and D in Figs. 3(b) and 3(c) from the closed-form expressions in Eqs. (13) and (14). From Fig. 3(b), we notice that σ is also more sensitive to L than D, similar to κ in Fig. 3(a). Furthermore, σ is observed to increase sharply with L when $L < 20$ nm but starts to saturate to the bulk value for larger L. The contrast between the slow, smooth drop for κ in Fig. 3(a) across the full range of L and the sharper collapse for σ in Fig. 3(b) for $L < 20$ nm results in a window where the PGEC concept of Fig. 1(b) can be realized. To better understand these trends, we provide a scaling analysis of κ,σ with D,L in the following section. Meanwhile, from Fig. 3(c) the Seebeck coefficient S is not affected by the variations of L and D in the classical model used here. This can be understood from Eq. (14), which shows that S depends only on the reduced Fermi level and the scattering mechanisms. Since $r = -1/2$ for both electron-phonon and electron-defect scattering, for a given dopant concentration and temperature, the reduced Fermi level is fixed, and S is independent of the absolute scattering time and thus the defect density.

When combined together, the thermal and electrical properties in Figs. 3(a)–3(c) lead to a figure of merit ZT as shown in Fig. 3(d). As L decreases, ZT can be enhanced 18-fold compared to bulk silicon, reaching as high as $ZT \approx 0.5$ for $L \approx 11$ nm, $D \approx 5$ nm. This value may even underestimate the actual attainable ZT by nearly a factor of 2 since κ is overestimated by the same amount using the Tersoff potential.

Even greater ZT can be achieved at higher temperatures with corresponding optimized doping concentration. Such temperature effects and possible bipolar contributions may be interesting considerations for future investigations. In the silicon metamaterial both electrical and thermal conductivities are reduced by the patterned defective regions, but ZT is set by the ratio of electrical to thermal properties, rather than their individual absolute values. For small L, σ grows faster than κ, and the material is more "crystalline" for electrons than for phonons. Therefore, as surmised, the regularly patterned defects can achieve a PGEC with $\Lambda_e < L < \Lambda_p$.

Another interesting aspect pertains to the ordered distribution of the defective regions and the possible effects of disrupting this order (were the damaged regions arranged in a nonregular way). The effects of disordered structures were considered for nanoporous silicon [20,32], which suggested that disordered pores would not change thermal conductivity appreciably and also that an ordered arrangement of pores is not required to maintain electronic conduction properties. This is consistent with our kinetic theory analysis, where the defect sites do not need to be ordered, as long as the mean spacing between defective areas falls into the length window between the mean free path of electrons and that of phonons.

B. Sensitivity of thermoelectric properties to L and D

In this section, we present a scaling analysis to understand both the greater sensitivity of κ and σ to L than D and the more rapid recovery of σ than κ as L increases. Both κ and σ can be written as a function of D and L,

$$\zeta(D,L) = b(D,L)\Lambda(D,L), \tag{15}$$

where $\zeta = \kappa$ or σ, $b(D,L)$ accounts for the changes in band structure for both phonons and electrons, and $\Lambda(D,L)$ is the mean free path. In the following, we assume the band function $b(D,L)$ is constant and insensitive to D and L, which is accurate when $D \ll L$ or D and L vary in a narrow range, as considered in this work.

Therefore, the sensitivity can be defined as

$$\frac{\partial \zeta}{\partial (D,L)} = \frac{\partial \zeta}{\partial \Lambda}\frac{\partial \Lambda}{\partial (D,L)}, \tag{16}$$

where $\partial(D,L)$ denotes the partial derivative with respect to D or L. Similar to Eq. (5), Matthiessen's law for the mean free path can be written as

$$\Lambda(D,L) = \frac{\Lambda_i \Lambda_D(D,L)}{\Lambda_i + \Lambda_D(D,L)}. \tag{17}$$

Note that Λ_i represents the intrinsic mean free path in pristine silicon and is assumed to be insensitive to (D,L). Substituting Eq. (17) into Eq. (16),

$$\frac{\partial \zeta}{\partial (D,L)} = \left(\frac{\Lambda_i}{\Lambda_i + \Lambda_D}\right)^2 \frac{\partial \Lambda_D}{\partial (D,L)}. \tag{18}$$

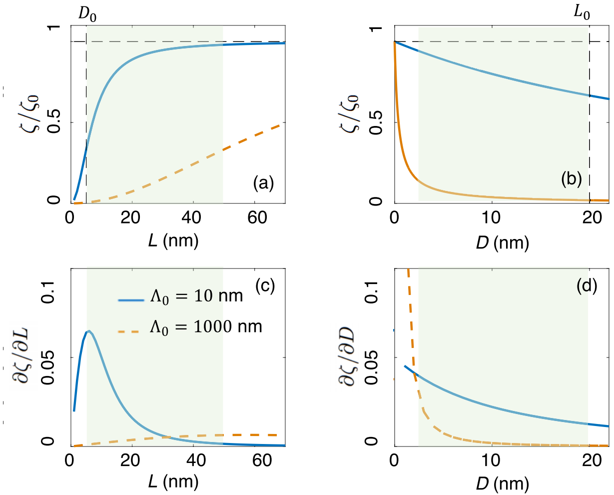

FIG. 4. Scaling of $\zeta = \kappa$ or σ as a function of (a) L and (b) D based on kinetic arguments for different intrinsic mean free paths Λ_0. While $\Lambda_0 = 10$ nm represents the scaling of electron conductivity, $\Lambda_0 = 1000$ nm approximates the trend of phonon conductivity. For direct comparison the values of L and D are given with dimensions. The shaded areas signify the parameter ranges considered in this work. (c) and (d) Sensitivity to L and D. In the range of L, κ keeps increasing, and σ saturates earlier. Meanwhile, for the considered range of D, the conductivities are similarly sensitive to D and L. These results are consistent with the trends in Figs. 3(a) and 3(b).

Applying Eq. (12) for τ_D,

$$\frac{\partial \zeta}{\partial D} \sim \left(\frac{\Lambda_i}{\Lambda_i + L^2/2D}\right)^2 \frac{L^2}{2D^2}, \tag{19}$$

$$\frac{\partial \zeta}{\partial L} \sim \left(\frac{\Lambda_i}{\Lambda_i + L^2/2D}\right)^2 \frac{L}{D}. \tag{20}$$

These scaling forms and corresponding sensitivity are shown in Fig. 4. Two sets of results are shown for intrinsic mean free paths $\Lambda_0 = 10$ nm and $\Lambda_0 = 1000$ nm. The former represents Λ_e, while the latter represents Λ_p in silicon. In the relevant ranges of D and L, we observe a similar sensitivity of σ and κ to L and D. This scaling analysis also recovers the early saturation in σ for $L > 20$ nm compared to κ. These trends are consistent with those in Figs. 3(a) and 3(b).

IV. CONCLUSION

We showed that regularly patterned nanoscale defects formed by ion beam irradiation in silicon can be used to realize a phonon-glass electron-crystal, which is of interest for thermoelectric applications. When the distance between the patterned defects lies within the length window of electron and phonon mean free paths, the thermal conductivity can be reduced without substantial detriment to the electrical properties. Using the Green-Kubo relations and equilibrium molecular dynamics, we predicted a 19-fold reduction in κ. Meanwhile, with Boltzmann theory the electrical power factor was shown to retain more than 80% of its value in crystalline silicon. To apply Boltzmann theory we used partial-wave analysis to derive a scattering model for electrons in a cylindrical potential. Combining these predictions, we obtained a $ZT \approx 0.5$ or

greater at room temperature. In consideration of economic and manufacturing aspects, silicon has been chosen as a representative material. However, the physical trends observed may apply to other materials as well, particularly those with longer phonon mean free paths.

ACKNOWLEDGMENTS

We gratefully acknowledge J. Ma and Emil Annevelink from the University of Illinois at Urbana-Champaign for helpful discussions. We acknowledge financial support from the National Science Foundation under Grant No. EAGER-1550895. Computational resources were provided by both (i) the Blue Waters sustained petascale computing facilities and (ii) the Illinois Campus Computing Cluster.

APPENDIX A: GRAPHICAL APPROACH FOR FERMI LEVEL AND CHARGE DENSITY

We employed the graphical iteration method to determine the Fermi level and carrier density for bulk silicon [35]. This method is based on the principle of charge neutrality, $n^- = n^+$, where $n^- = n_e + n_a^-$ is the sum of electron and ionized acceptor concentrations and $n^+ = n_h + n_d^+$ is the total of hole and ionized donor concentrations. Fermi-Dirac statistics gives

$$n_a^- = n_a \Big/ \left(1 + 2\exp\frac{E_a - \mu}{k_B T}\right)$$

and

$$n_d^+ = n_a \Big/ \left(1 + 2\exp\frac{\mu - E_d}{k_B T}\right),$$

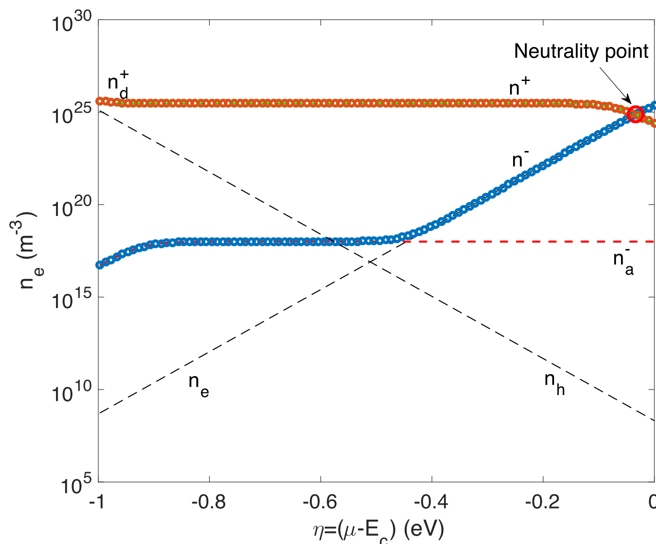

FIG. 5. The graphical iteration method for the determination of the Fermi level. The charge-neutrality point is indicated by the red circle. This approach gives carrier density and Fermi level simultaneously. In this case, electron density is 7.5×15 cm^{-3}, and Fermi level is 34 meV below CBM.

where E_a and E_d are ionization energies and n_e and n_h are intrinsic carrier densities, defined by

$$n_e = 2(m_e^* k_B T/2\pi\hbar^2)^{3/2} \exp\frac{\mu - E_c}{k_B T}$$

and

$$n_h = 2(m_h^* k_B T/2\pi\hbar^2)^{3/2} \exp\frac{E_v - \mu}{k_B T},$$

where E_c and E_v are the conduction-band minimum (CBM) and valence-band maximum. The graphical method searches for the charge-neutrality point graphically considering all these contributions to the charge density. In Fig. 5, we give the case of $T = 300$ K and phosphorous doping at concentrations of $n_P = 3 \times 16$ cm^{-3} and $n_{Al} = 1 \times 9$ cm^{-3}. The ionization energies of phosphorous and aluminum in silicon are 45 and 57 meV, respectively. Notice that this approach gives two important quantities simultaneously: carrier density and Fermi level. In this case, the electron density is 7.5×15 cm^{-3}, and the Fermi level is 34 meV below the CBM.

APPENDIX B: SCATTERING CROSS SECTION FROM PARTIAL-WAVE ANALYSIS

For the azimuthally symmetric potential in Eq. (6), an incident plane wave $\psi_i(z) = A\exp(i\mathbf{k}\cdot\mathbf{r})$ is expected to be scattered into a spherical wave (see, for example, [38]),

$$\psi_S(r) = Af(k,\theta)\frac{\exp(ikr)}{r}, \tag{B1}$$

where $f(k,\theta)$ is the scattering amplitude, and a composite wave field

$$\psi(r) = \psi_i(r) + \psi_S(r) \tag{B2}$$

should be sought as the solution to the Schrödinger equation

$$\left[\nabla^2 + k^2 - \frac{2m}{\hbar^2}V(r)\right]\psi(r) = 0, \tag{B3}$$

where $k^2 = 2m\epsilon/\hbar^2$. The time-independent form is employed since the scattering is assumed to be elastic, and thus, energy remains unchanged during scattering.

The probability of the incident particle with speed v passing through an infinitesimal area $d\sigma$ in time dt is $dP = |A|^2 v dt d\sigma$, which is equal to the probability of scattering into the corresponding solid angle $d\Omega$, $dP = |A|^2|f(k,\theta)|^2 v dt r^2 d\Omega$. Thus, by definition the differential scattering cross section is

$$\sigma_m(\theta) = |f(k,\theta)|^2. \tag{B4}$$

Therefore, to determine the scattering rate τ_D^{-1} in Eq. (7), we need only to calculate the scattering amplitude $f(k,\theta)$ in Eq. (B1). For this, two possible methods are partial-wave analysis and the Born approximation. However, the latter assumes a small scattering potential so that the scattering field is only slightly changed from the incident wave field. Since the ion beam patterned regions are expected to introduce substantial scattering, it is necessary to consider large scattering barriers for which the Born approximation becomes singular. Therefore, we derive the scattering cross section and momentum relaxation using partial-wave expansion, which remains valid.

The partial-wave method decomposes the incident and scattered wave functions into partial spherical waves and then imposes boundary conditions to determine the partial-wave magnitudes or phase shifts for each (see, for example, Ref. [38]). Based on partial-wave analysis for the azimuthally symmetric potential, the differential cross section is formulated as

$$\sigma(\theta) = \frac{1}{k^2}\left|\sum_{l=0}^{\infty}(2l+1)e^{i\delta_l}\sin\delta_l P_l(\cos\theta)\right|^2, \tag{B5}$$

where δ_l is the phase shift between incident and scattered waves and P_l is the lth Legendre polynomial. The scattering process can be completely determined if the phase shifts δ_l are known for all partial waves. However, this method is particularly useful when dealing with low-energy scattering ($ka \ll 1$), where only the first term ($l = 0$, the so-called S wave) dominates. We consider in this work S-wave scattering, which is also consistent with the assumption of isotropic scattering as required by Boltzmann theory [36,37]. In other words, based on the definition in Eq. (8),

$$\sigma_m = \frac{4\pi}{k^2}\sin^2\delta_0. \tag{B6}$$

The solution of the Schödinger equation [Eq. (B3)] thus formulated is separable, and the radial components of the equation are

$$\begin{aligned} \frac{du^2}{dr^2} + (k^2 - k_0^2)u = 0, \quad r \leqslant a, \\ \frac{du^2}{dr^2} + k^2u = 0, \quad r > a, \end{aligned} \tag{B7}$$

where $k^2 = 2m\epsilon/\hbar^2$ and $k_0^2 = 2mV_0/\hbar^2$. The solutions are

$$u(r) = \begin{cases} A\sinh(k_1r), & r \leqslant a, \\ B\sin(kr+\delta_0), & r > a, \end{cases} \tag{B8}$$

where $k_1^2 = k_0^2 - k^2$. Imposing the continuity of wave functions and their derivatives at $r = a$ gives

$$A\sinh(k_1a) = B\sin(kr+\delta_0), \tag{B9a}$$

$$Ak_1\cosh(k_1a) = Bk\cos(kr+\delta_0). \tag{B9b}$$

Dividing the two equations above, we obtain

$$\tan\delta_0 = \frac{k\tanh(k_1a) - k_1\tan(ka)}{k_1 + k\tan(ka)\tanh(k_1a)}. \tag{B10}$$

Using Eqs. (B6) and (B10), the scattering cross section can be determined as

$$\sigma_m = \frac{4\pi a^2}{(ka)^2}\sum_{l=0}^{N_l\to\infty}(2l+1)\left|\frac{j_l(ka)}{h_l^{(1)}(ka)}\right|^2, \tag{B11}$$

where j_l and $h_l^{(1)}$ are the spherical Bessel and first-kind Hankel functions. In the limits of low carrier energy $ka \ll 1$ and high barrier $k_1a \gg 1$, we have $k_1a \approx k_0a$, and the above equation can be simplified to

$$\tan\delta_0 \approx \delta_0 \approx k\left(\frac{\tanh(k_0a) - k_0a}{k_0}\right) \approx -ka \tag{B12}$$

and

$$\sigma_m \approx 4\pi a^2\left(1 - \frac{\tanh(k_0a)}{k_0a}\right)^2 \approx 4\pi a^2, \tag{B13}$$

which is Eq. (9) in the main text.

[1] A. Majumdar, Science 303, 777 (2004).
[2] T. M. Tritt and M. Subramanian, MRS Bull. 31, 188 (2006).
[3] J. R. Sootsman, D. Y. Chung, and M. G. Kanatzidis, Angew. Chem., Int. Ed. 48, 8616 (2009).
[4] A. Minnich, M. Dresselhaus, Z. Ren, and G. Chen, Energy Environ. Sci. 2, 466 (2009).
[5] J. P. Heremans, M. S. Dresselhaus, L. E. Bell, and D. T. Morelli, Nat. Nanotechnol. 8, 471 (2013).
[6] G. S. Nolas, J. Sharp, and J. Goldsmid, *Thermoelectrics: Basic Principles and New Materials Developments*, Springer Series in Materials Science Vol. 45 (Springer, Berlin, 2013).
[7] A. A. Balandin, J. Nanosci. Nanotechnol. 5, 1015 (2005).
[8] L. D. Hicks and M. S. Dresselhaus, Phys. Rev. B 47, 12727 (1993).
[9] M. S. Dresselhaus, G. Chen, M. Y. Tang, R. Yang, H. Lee, D. Wang, Z. Ren, J.-P. Fleurial, and P. Gogna, Adv. Mater. 19, 1043 (2007).
[10] G. A. Slack, in *CRC Handbook of Thermoelectrics*, edited by D. M. Rowe (CRC Press, Boca Raton, FL, 1995), Chap. 34, pp. 407–440.
[11] H. Liu, X. Yuan, P. Lu, X. Shi, F. Xu, Y. He, Y. Tang, S. Bai, W. Zhang, L. Chen *et al.*, Adv. Mater. 25, 6607 (2013).
[12] R. Venkatasubramanian, E. Siivola, T. Colpitts, and B. O'Quinn, Nature (London) 413, 597 (2001).
[13] T. Harman, P. Taylor, M. Walsh, and B. LaForge, Science 297, 2229 (2002).
[14] G. J. Snyder and E. S. Toberer, Nat. Mater. 7, 105 (2008).
[15] G. Nolas, D. Morelli, and T. M. Tritt, Annu. Rev. Mater. Sci. 29, 89 (1999).
[16] T. Zhu, C. Fu, H. Xie, Y. Liu, and X. Zhao, Adv. Energy Mater. 5, 1500588 (2015).
[17] S. LeBlanc, S. K. Yee, M. L. Scullin, C. Dames, and K. E. Goodson, Renewable Sustainable Energy Rev. 32, 313 (2014).
[18] A. I. Hochbaum, R. Chen, R. D. Delgado, W. Liang, E. C. Garnett, M. Najarian, A. Majumdar, and P. Yang, Nature (London) 451, 163 (2008).
[19] S. K. Bux, R. G. Blair, P. K. Gogna, H. Lee, G. Chen, M. S. Dresselhaus, R. B. Kaner, and J.-P. Fleurial, Adv. Funct. Mater. 19, 2445 (2009).
[20] J.-H. Lee, G. A. Galli, and J. C. Grossman, Nano Lett. 8, 3750 (2008).
[21] S. K. Yee, S. LeBlanc, K. E. Goodson, and C. Dames, Energy Environ. Sci. 6, 2561 (2013).
[22] K. Swaminathan-Gopalan, T. Zhu, E. Ertekin, and K. A. Stephani, Phys. Rev. B 95, 184109 (2017).
[23] J. Tang, H.-T. Wang, D. H. Lee, M. Fardy, Z. Huo, T. P. Russell, and P. Yang, Nano Lett. 10, 4279 (2010).

[24] J. A. Perez-Taborda, M. M. Rojo, J. Maiz, N. Neophytou, and M. Martin-Gonzalez, Sci. Rep. **6**, 32778 (2016).
[25] M. Zebarjadi, K. Esfarjani, A. Shakouri, J.-H. Bahk, Z. Bian, G. Zeng, J. Bowers, H. Lu, J. Zide, and A. Gossard, Appl. Phys. Lett. **94**, 202105 (2009).
[26] A. I. Boukai, Y. Bunimovich, J. Tahir-Kheli, J.-K. Yu, W. A. Goddard III, and J. R. Heath, Nature **451**, 168 (2008).
[27] J. A. Anderson, C. D. Lorenz, and A. Travesset, J. Comput. Phys. **227**, 5342 (2008).
[28] J. Tersoff, Phys. Rev. B **38**, 9902 (1988).
[29] J. F. Ziegler, J. Biersack, and U. Littmark, *The Stopping and Range of Ions in Matter* (Pergamon, New York, 1985), Vol. 1.
[30] D. Frenkel and B. Smit, *Understanding Molecular Simulation: From Algorithms to Applications* (Academic, San Diego, 2001), Vol. 1.
[31] W. Fulkerson, J. Moore, R. Williams, R. Graves, and D. McElroy, Phys. Rev. **167**, 765 (1968).
[32] J. Lee, J. Grossman, J. Reed, and G. Galli, Appl. Phys. Lett. **91**, 223110 (2007).
[33] M. Lundstrom, *Fundamentals of Carrier Transport* (Cambridge University Press, Cambridge, 2009).
[34] J. Ma and S. Sinha, J. Appl. Phys. **112**, 073719 (2012).
[35] C. Kittel, *Introduction to Solid State Physics* (Wiley, Hoboken, NJ, 2005).
[36] C. Jacoboni, *Theory of Electron Transport in Semiconductors: A Pathway from Elementary Physics to Nonequilibrium Green Functions*, Springer Series in Solid-State Sciences Vol. 165 (Springer, Berlin, 2010).
[37] C. M. Wolfe, N. Holonyak, Jr., and G. E. Stillman, *Physical Properties of Semiconductors* (Prentice-Hall, Englewood Cliffs, NJ, 1988).
[38] L. I. Schiff, *Quantum Mechanics* (McGraw-Hill, New York, 1968).
[39] B. Graczykowski, A. El Sachat, J. Reparaz, M. Sledzinska, M. Wagner, E. Chavez-Angel, Y. Wu, S. Volz, Y. Wu, F. Alzina *et al.*, Nat. Commun. **8**, 415 (2017).
[40] Y. Xu, Z. Lin, X. Zhong, X. Huang, N. O. Weiss, Y. Huang, and X. Duan, Nat. Commun. **5**, 4554 (2014).
[41] Y. Lin, X. Han, C. J. Campbell, J.-W. Kim, B. Zhao, W. Luo, J. Dai, L. Hu, and J. W. Connell, Adv. Funct. Mater. **25**, 2920 (2015).
[42] R. L. Liboff, *Kinetic Theory: Classical, Quantum, and Relativistic Descriptions* (Springer, Berlin, 2003).
[43] T. Zhu, K. Swaminathan-Gopalan, K. Stephani, and E. Ertekin, Adv. Funct. Mater. **28**, 1706268 (2018).